Research
Metamaterials—Article

A Planar 4-Bit Reconfigurable Antenna Array Based on the Design Philosophy of Information Metasurfaces

Zheng Xing Wang [a,b], Hanqing Yang [a,b], Ruiwen Shao [a,b], Jun Wei Wu [a,b], Guobiao Liu [a,b], Feng Zhai [a,b], Qiang Cheng [a,b,*], Tie Jun Cui [a,b,*]

[a] State Key Laboratory of Millimeter Waves, School of Information Science and Engineering, Southeast University, Nanjing 210096, China
[b] The Institute of Electromagnetic Space, Southeast University, Nanjing 210096, China

A R T I C L E   I N F O

A B S T R A C T

Inspired by the design philosophy of information metasurfaces based on the digital coding concept, a planar 4-bit reconfigurable antenna array with low profile of $0.15\lambda_0$ (where λ_0 is the free-space wavelength) is presented. The array is based on a digital coding radiation element consisting of a 1-bit magnetoelectric (ME) dipole and a miniaturized reflection-type phase shifter (RTPS). The proposed 1-bit ME dipole can provide two digital states of "0" and "1" (with 0° and 180° phase responses) over a wide frequency band by individually exciting its two symmetrical feeding ports. The designed RTPS is able to realize a relative phase shift of 173°. By digitally quantizing its phase in the range of 157.5°, additional eight digital states at intervals of 22.5° are obtained. To achieve low sidelobe levels, a 1:16 power divider based on the Taylor line source method is employed to feed the array. A prototype of the proposed 4-bit antenna array has been fabricated and tested, and the experimental results are in good agreement with the simulations. Scanning beams within a ±45° range were measured with a maximum realized gain of 13.4 dBi at 12 GHz. The sidelobe and cross-polarization levels are below –14.3 and –23.0 dB, respectively. Furthermore, the beam pointing error is within 0.8°, and the 3 dB gain bandwidth of the broadside beam is 25%. Due to its outstanding performance, the array holds potential for significant applications in radar and wireless communication systems.

© 2022 THE AUTHORS. Published by Elsevier LTD on behalf of Chinese Academy of Engineering and Higher Education Press Limited Company. This is an open access article under the CC BY-NC-ND license (http://creativecommons.org/licenses/by-nc-nd/4.0/).

1. Introduction

Electronic beam-scanning arrays with high gains and low sidelobes are useful for radar, mapping, communications, and so on [1]. Conventional phased arrays are usually regarded as strong competitors in these applications due to their superior ability in electronic speed, inertia-less scanning, and multiple target tracking [2]. However, it is common to use solid-state transmit–receive (T/R) modules at the subarray or even element level in traditional phased arrays. In addition, complicated feed and beamforming architectures must be used [1]. These factors undoubtedly increase the cost, weight, and complexity of phased arrays, preventing their application in scenarios that require lower cost and lighter weight.

Great progress has been made in information metasurfaces, including digital coding and programmable metasurfaces, since their first exhibition in 2014 [3–16]. The design philosophy of information metasurfaces is applying the digital coding concept to their configuration [3,4]. For example, in the original 1-bit information metasurface, the digital states "0" and "1" are used to represent two distinct coding elements with a 180° phase difference [5]. This concept was subsequently extended from 1-bit coding to multi-bit coding by multi-level discretization of the 360° phase [6]. The digital representation of metasurfaces has the merits of simplifying the design and optimization procedures [7]. It also makes it possible to revisit metasurfaces from the perspective of information science, which builds up a bridge between the physical world and the digital world [3,4]. Due to the revolutionary progress that has been made with information metasurfaces, they hold promise for applications in wireless communication systems [13–16].

Inspired by the design philosophy of information metasurfaces (i.e., the digital coding concept), reconfigurable bit arrays utilizing digital elements to achieve beam scanning have been proposed in order to reduce cost and complexity [17–26]. Reconfigurable bit reflectarrays [17,18] and transmitarrays [19–21] have been well

---

accepted because of their real-time beam agility and high gains. However, like most information metasurfaces [3–16], they are actually three-dimensional (3D) structures due to the feeding source and support, which restricts their applications in space-limited scenarios. In response to demands for a lower profile and simpler architecture, planar reconfigurable bit arrays have been proposed [22–26]. Planar 1-bit arrays were designed in Refs. [22–24], but they can only steer two scanning beams that are neither orthogonal nor independent, making them almost useless in radar and communication systems. Later, planar 2-bit arrays, including a reconfigurable traveling-wave antenna array and a circularly polarized beam-steering antenna array, were presented [25,26]. Both of the arrays can steer a single scanning beam. Nevertheless, it should be pointed out that, although the beam-scanning scheme of reconfigurable bit arrays is simplified by means of the digital coding method, the cost is the deterioration of radiation performance [27,28]. Accordingly, planar arrays with 2-bit phase quantization inevitably give rise to non-negligible beam pointing errors and quantization lobes [25,26]. In order to alleviate the quantization error, an effective method is to increase the number of quantization bits. In addition, most of the above reconfigurable bit arrays have narrow bandwidths [18,20,24–26], which hinders their practical applications in engineering.

In this work, a planar 4-bit reconfigurable antenna array is proposed. We first design a digital coding radiation element by combining a 1-bit magnetoelectric (ME) dipole and a miniaturized reflection-type phase shifter (RTPS). The ME dipole is selected due to its advantages of a symmetrical radiation pattern, wide bandwidth, and low backlobe [29,30]. A π-shaped probe with two symmetrical switchable feed ports is utilized to excite the dipole. With the ports excited individually, an intrinsic phase shift of 180° can be obtained due to their relative spatial position [31]. The technique employed to generate the spatial phase shift is similar to the sequential rotation (SR) technique, which is commonly used in wideband circularly polarized arrays [31–35]. The introduction of the spatial phase shift brings two benefits. One is a stable phase difference (180°) over a wide bandwidth, and the other is a relatively compact structure compared with the 180° phase delay line [24]. In addition to the 1-bit ME dipole, a miniaturized RTPS [36,37] is designed to provide additional eight discrete phase states. Thus, the digital coding radiation element is formed, which is able to realize a phase shift of 337.5° in steps of 22.5°. Furthermore, a planar 4-bit reconfigurable antenna array along the H plane is designed based on the digital coding radiation element. To achieve a low sidelobe level, a 1:16 power divider, whose amplitude distribution is calculated by the Taylor line source method [2], is utilized to feed the array. The proposed 4-bit array inherits the advantages of planar reconfigurable bit arrays, such as light weight, low cost, and low profile. Moreover, both simulations and measurements verify its excellent scanning performance, high gain, low sidelobe, and wide bandwidth.

2. Digital coding radiation element

2.1. 1-bit ME dipole

The geometrical configuration and parameters of the 1-bit ME dipole are shown in Fig. 1. The dipole is composed of two layers: the radiation layer and the feed layer. The substrate of the radiation layer is realized by gluing two layers of 1.524 mm-thick Rogers RO4350B (ε_r = 3.66 and $\tan\delta$ = 0.0037 at 12 GHz; where ε_r and $\tan\delta$ are relative permittivity and tangential loss, respectively) laminates with 0.2 mm-thick RO4450F (ε_r = 3.70 and $\tan\delta$ = 0.0040 at 12 GHz) bondply. The substrate of the feed layer is 0.254 mm-thick Rogers RO4350B. The radiation and feed layers
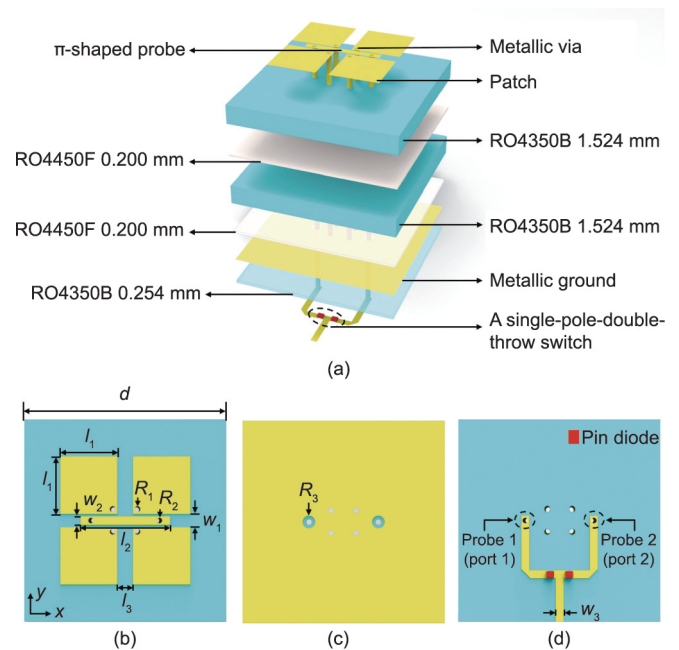

Fig. 1. Geometry of the proposed 1-bit ME dipole: (a) 3D view; (b) top view; (c) metallic ground; and (d) bottom view. d = 13 mm, l_1 = 3.7 mm, w_1 = 0.85 mm, l_2 = 5.8 mm, w_2 = 0.55 mm, l_3 = 1 mm, w_3 = 0.52 mm, R_1 = R_2 = 0.2 mm, R_3 = 0.4 mm.

share the same metallic ground and are bonded together with 0.2 mm-thick RO4450F Bondply. As shown in Figs. 1(a) and (b), the dipole consists of four square patches, four metallic vias, and a π-shaped probe. The four square patches, which are positioned about $\lambda_g/4$ (where λ_g is the wavelength in the substrate at 12 GHz) above the metallic ground, have a width of l_1 and perform as two planar electric dipoles along the x-axis. Each square patch has a via hole with a radius of R_1, which is connected to the metallic ground plane. The four metallic vias, together with the metallic ground, can be viewed as an equivalent magnetic dipole. They form a loop current and radiate through two apertures between the metallic patches along the y-axis. The π-shaped probe is utilized to feed the ME dipole, which is composed of two symmetrical switchable probes with a radius of R_2 and a rectangular patch with the dimensions of $l_2 \times w_2$. Fig. 1(c) displays the shared metallic ground, and the radius of the defected ground is R_3. To switch between the two feed probes, the π-shaped probe is connected to a single-pole-double-throw (SPDT) switch on the feed layer, whose detailed layout is drawn in Fig. 1(d). The SPDT switch has two switchable ports that are implemented by integrating two pin diodes (MADP-000907-14020W) [38] into a microstrip line with a width of w_3. When a positive or negative direct current (DC) voltage is supplied to the pin diodes, the two ports can then be individually switched on.

Full-wave simulations of the ME dipole were performed in Computer Simulation Technology (CST) Microwave Studio [39], wherein the structure was strictly modeled. In the simulations, the pin diode is modeled as a lumped circuit element, whose parallel resistor (R)–inductor (L)–capacitor (C) (RLC) parameters for the ON and OFF states are R = 15 Ω, L = 1187 nH, and C = 1.29 pF, and R = 4000 Ω, L = 2250 nH, and C = 0.028 pF, respectively. We briefly introduce the extraction of the circuital parameter values of the pin diode here. Firstly, the amplitudes and phases for the ON and OFF states are measured by the test fixture. Next, equivalent circuit models composed of a resistor R, an inductor L, and a capacitor C are utilized to characterize the pin diode. Finally, the amplitude and phase results of the equivalent circuit models are fitted in the commercial Advanced Design System (ADS) circuit

simulation software, and the circuital parameter values are obtained. Since the optimization of equivalent circuit models in ADS circuit simulation software is conducted in a wide frequency band, the accuracy of the models can be guaranteed in the corresponding band. The 1-bit ME dipole has two distinct working states. The "0" state is defined when port 1 is switched off and port 2 is switched on, while the "1" state is defined the other way around. The simulated $|S_{11}|$ of the two states are illustrated in Fig. 2(a) and are exactly the same due to the symmetry of the structure. In addition, a wide impedance bandwidth of 36.2% (with $|S_{11}| <$ −10 dB from 9.5 to 13.7 GHz) can be achieved for both states.

To investigate the phase difference between the two states in the simulations, an *x*-oriented probe is placed in the far-field region of the dipole to record its electric field. As shown in Fig. 2(b), a 180° phase difference is obtained. Furthermore, the phase difference is stable over a broad frequency band, thanks to the use of spatial phase shift. Figs. 2(c) and (d) displays surface current distributions on the dipole for the two states at 12 GHz. It is clear that the current directions of the "0" and "1" states are exactly opposite at the same time (*t* = 0), which further demonstrates the existence of a 180° phase difference between the two states. Figs. 3(a) and (b) shows the radiation patterns of the ME dipole at 12 GHz when it works on the "0" state. For both the E and H planes, the broadside radiation patterns are symmetrical, and the 3 dB beamwidth in the two planes is 86° and 94°, respectively. Moreover, the simulated realized gain is up to 5.5 dBi, and the cross-polarization level (*y*-polarized) is less than −30 dB. From Fig. 3(c), it can be seen that the realized gain is stable from 10 to

13 GHz, with a variation of less than 1 dB. Furthermore, the front-to-back ratio is greater than 15 dB over the major portion of the working band. In the vicinity of the higher end of the band, the ratio decreases to 13 dB. The variation of the front-to-back ratio in Fig. 3(c) is due to two factors. The first of these factors is the back radiation of the feed network. The other factor is the defected ground shown in Fig. 1(c), which causes radiation leakage to the backward region. To solve this problem, a common method is to use a packaged microstrip line feeding network [40]. Although the front-to-back ratio varies with frequency, the value is still large enough over the whole frequency band; that is, the power radiated to the backward region is very small. Therefore, there are no dramatic changes in the gain results. As shown in Fig. 3(d), the radiation efficiency of the 1-bit ME dipole is 0.8 at 12 GHz.

2.2. Miniaturized RTPS

In addition to the 1-bit ME dipole, a miniaturized RTPS is designed to further provide the necessary phase shift for the 4-bit digital coding radiation element. Compared with the other two types of passive phase shifters—namely, the loaded transmission line and the switched network—the RTPS exhibits a good compromise between insertion loss and the range of phase variation [37]. Fig. 4(a) displays the proposed miniaturized RTPS, which consists of an improved 3 dB branch-line coupler connected with two identical loads at its through and coupled ports. Since compactness is of major importance for phase shifters, the two quarter-wavelength transmission lines of the RTPS adopt meander-line technology for miniaturization. The size of the RTPS can thus be
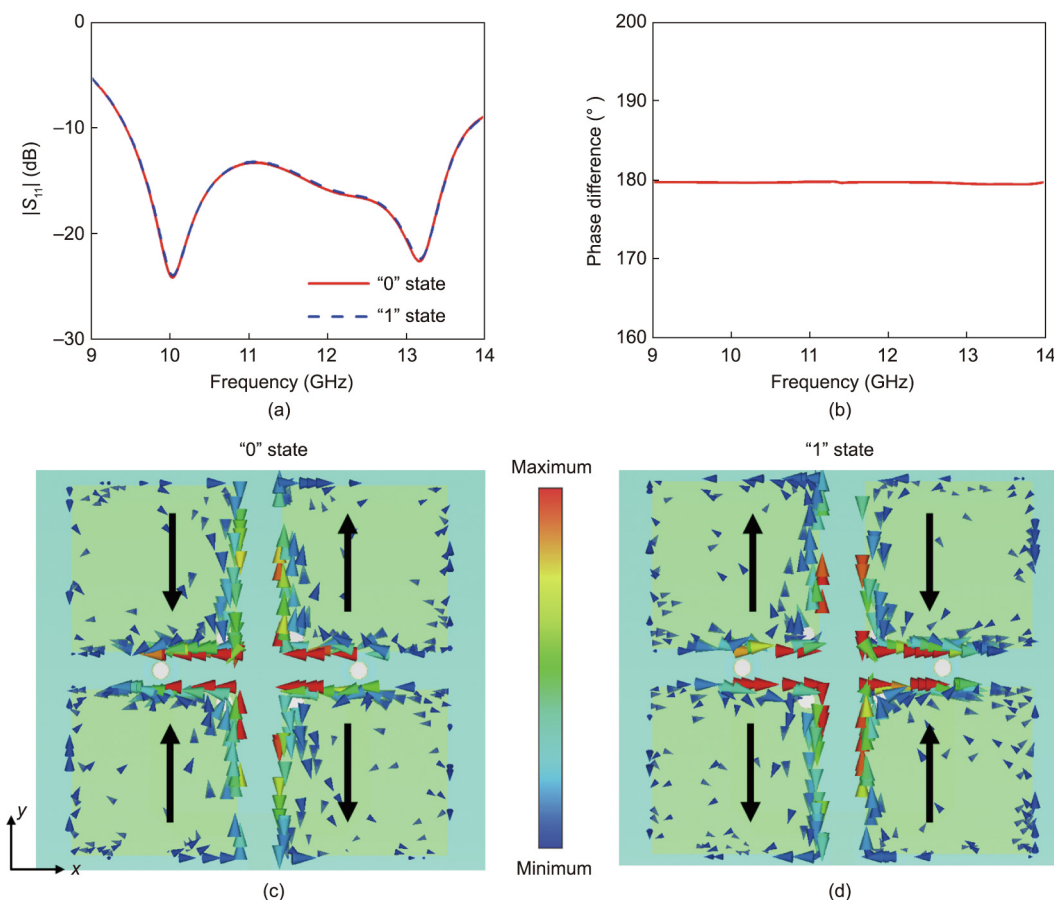

(a)

(b)

"0" state

"1" state

(c)

(d)

Fig. 2. Simulated performance of the 1-bit ME dipole. (a) Simulated $|S_{11}|$ for the two states; (b) phase difference between the "0" and "1" states; (c) simulated surface current distribution of the "0" state at 12 GHz; (d) simulated surface current distribution of the "1" state at 12 GHz.
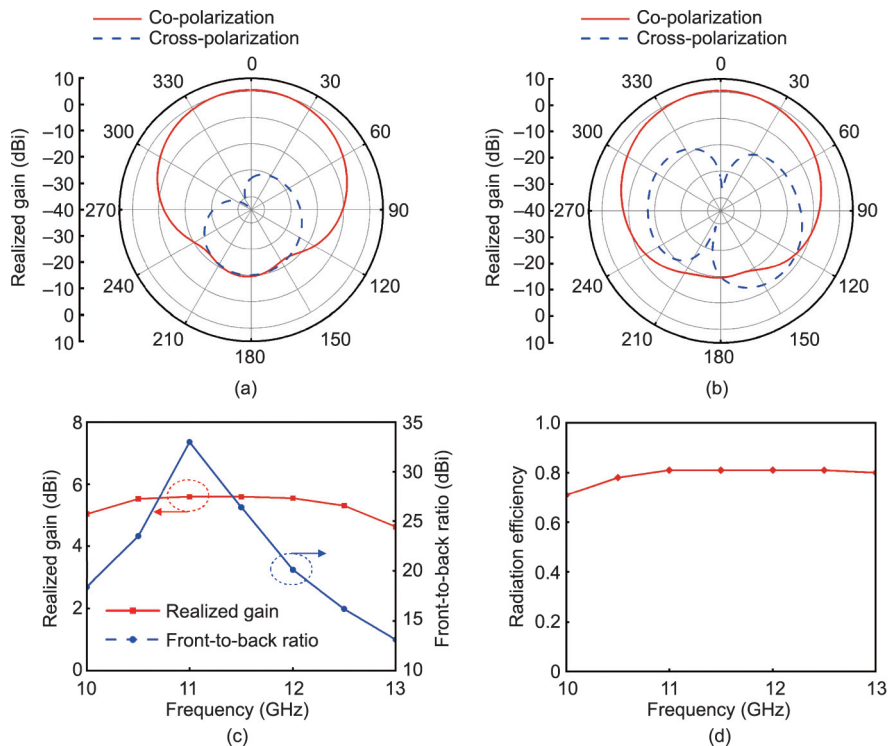
Fig. 3. Simulated radiation performance of the 1-bit ME dipole. (a) E plane pattern at 12 GHz; (b) H plane pattern at 12 GHz; (c) realized gain and front-to-back ratio; (d) radiation efficiency.
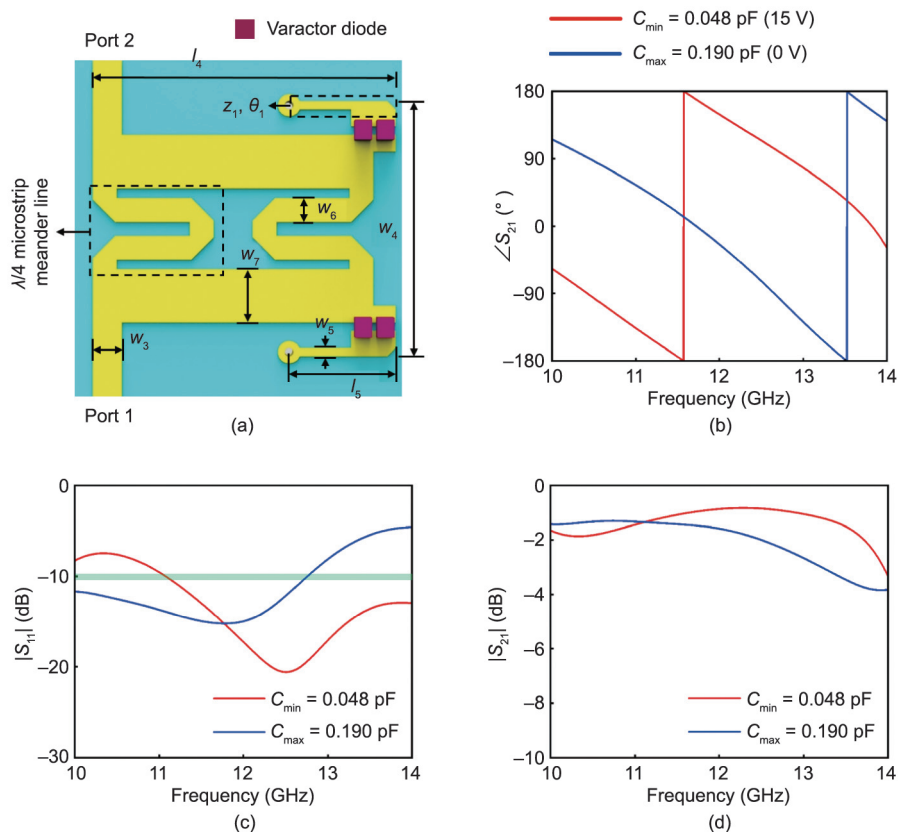

Fig. 4. Geometry and performance of the proposed RTPS. (a) Top view; (b) $\angle S_{21}$ for C_{min} and C_{max}; (c) $|S_{11}|$ for C_{min} and C_{max}; (d) $|S_{21}|$ for C_{min} and C_{max}. w_3 = 0.52 mm, w_4 = 4.5 mm, w_5 = 0.15 mm, w_6 = 0.43 mm, w_7 = 0.95 mm, l_4 = 5.4 mm, l_5 = 1.9 mm, z_1 = 97 Ω, θ_1 = 44°.

reduced to $0.18\lambda_0 \times 0.21\lambda_0$, where λ_0 is the free-space wavelength at 12 GHz. Each load of the RTPS is made up of two parallel varactor diodes (MAVR-011020-1411) [41] and a transmission line shorted to the ground. The characteristic impedance and electrical length of the line are Z_1 and θ_1, respectively. In the simulations, the varactor diode is modeled by a capacitor C in series with a parasitic resistance R, which accounts for the main contribution to the loss of the RTPS. The designed RTPS is a two-port network, and its scattering matrix has the following form [42]:

$$\boldsymbol{S} = \frac{1}{\sqrt{2}}\begin{pmatrix} i & -1 \\ -1 & i \end{pmatrix} \cdot \begin{pmatrix} \Gamma & 0 \\ 0 & \Gamma \end{pmatrix} \cdot \frac{1}{\sqrt{2}}\begin{pmatrix} i & -1 \\ -1 & i \end{pmatrix} = \begin{pmatrix} 0 & -i\Gamma \\ -i\Gamma & 0 \end{pmatrix} \quad (1)$$

where Γ is the reflection coefficient at the loaded ports. Hence, the transmission parameter S_{21} of the RTPS is equal to $-i\Gamma$, and the insertion loss is then obtained by the following:

$$|S_{21}| = -20\log|\Gamma| \quad (2)$$

The phase shift $\Delta\varphi$ of the RTPS is given by the following equations:

$$\Delta\varphi = \angle S_{21}|_{C_{min}} - \angle S_{21}|_{C_{max}} \quad (3)$$

and

$$\angle S_{21} = -90° + \angle\Gamma \quad (4)$$

A detailed derivation of Γ can be found in the Appendix of Ref. [36]. According to the literature, the insertion loss is a function of R and decreases with decreasing R when the value of R is not too large. Thus, two varactor diodes are used in parallel in each load to reduce the total parasitic resistance, which reduces the insertion loss of the RTPS. Furthermore, it has been determined that the phase shift $\Delta\varphi$ is a function of θ_1, Z_1, and C [36]. Once the parameters of the transmission line in each load are fixed, the phase shift is determined by the range of C.

We optimize the structural parameters of the RTPS in CST Microwave Studio, and the final design geometries are given in Fig. 4. In the simulations, the parasitic resistance R of the varactor diode is set as 6 Ω, and the capacitance C varies in the range of 0.048–0.190 pF. As illustrated in Fig. 4(b), the simulated phase shift of the RTPS at 12 GHz is 173° when the capacitance varies from C_{min} = 0.048 pF (15 V) to C_{max} = 0.190 pF (0 V). The simulated reflection coefficients for the cases of C_{min} and C_{max} are shown in Fig. 4(c), and their overlapped impedance bandwidth is 13.3% for $|S_{11}|$ smaller than –10 dB (from 11.1 to 12.7 GHz). It can be seen in Fig. 4(d) that the insertion loss for C_{min} and C_{max} is 0.85 and 1.60 dB, respectively. In addition, the insertion loss increases with increasing frequency.

For a 4-bit reconfigurable array, each digital coding radiation element should have a quantized phase number of 16 (2^4). Two

phase states of 0° and 180° are supplied by the 1-bit ME dipole; thus, the RTPS just needs to provide another eight phase states. The simulated and measured phase shifts of the RTPS are normalized within the range of 0° to 180° and then are digitally quantized into eight phase states. The phase difference of each adjacent state is about 22.5°, as shown in Fig. 5(a). Corresponding simulated and measured insertion losses are illustrated in Fig. 5(b). It can be seen that the two results generally agree with each other, except that the measured ones indicate higher insertion losses. This may be due to the deviation of the varactor diodes' parasitic elements in the experiment and the parasitic effects caused by printed circuit board (PCB) prototyping and soldering. The minimum and maximum measured insertion losses are 1.0 and 2.4 dB, respectively, which is acceptable for a practical phase-shifter design. Based on the ME dipole and the RTPS, the 16 quantized phase states of the digital coding radiation element are listed in Table 1.

3. Planar 4-bit reconfigurable antenna array

Based on the above digital coding radiation element, a planar 4-bit reconfigurable antenna array was designed, as illustrated in Fig. 6. First, we propose a 1:16 power divider to feed the array. As shown in Fig. 6(a), the power divider is the parallel feed configuration and is designed based on a grounded coplanar waveguide (GCPW). Compared with a microstrip line, a GCPW transmission line has several advantages, including low radiation loss, low surface wave loss, and high mechanical strength. At the input and output ports of the power divider, GCPW-to-microstrip transitions are introduced to obtain impedance match with a sub-miniature-A (SMA) connector and radiation elements. Considering the isolation among the output ports and the compactness of the structure, a Wilkinson power divider is used as the input stage of the power divider, and T-junction dividers are utilized in the other stages. In order to achieve a low sidelobe level for the array, the 1:16 power divider is made with unequal power splits, thus generating a tapered amplitude distribution on the array from the center to the ends. The Taylor line source method is applied in the calculation of the amplitude distribution, and the goal for the sidelobe level and number of uniform sidelobes are set as –25 dB and 4, respectively. Table 2 provides the calculated, simulated, and measured amplitude distributions of the power divider at 12 GHz. Due to the symmetry of the structure, only the results for half of the ports are presented. As can be seen from the table, the three groups of data are in good agreement. Fig. 6(c) displays the simulated and measured reflection coefficients of the power divider. It is shown that the two results generally match with each other, except that the measured values increase around 11.1 and 12.0 GHz due to errors in the fabrication and soldering. Moreover, the simulated and measured phase differences among the eight
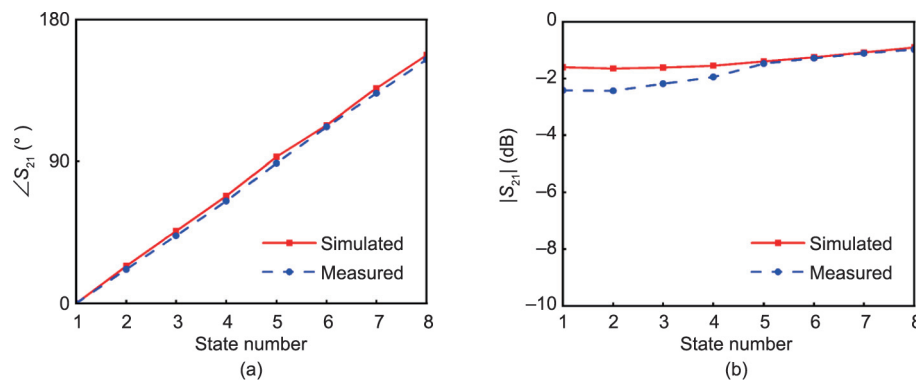

Fig. 5. Simulated and measured performance of the RTPS for the eight digital states at 12 GHz: (a) $\angle S_{21}$ and (b) $|S_{21}|$.

Table 1
Sixteen quantized phase states of the digital coding radiation element.

| Radiation element	1-bit ME dipole	RTPS	Phase	Radiation element	1-bit ME dipole	RTPS	Phase
State 0	"0" state	1	0°	State 8	"1" state	1	180.0°
State 1	"0" state	2	22.5°	State 9	"1" state	2	202.5°
State 2	"0" state	3	45.0°	State 10	"1" state	3	225.0°
State 3	"0" state	4	67.5°	State 11	"1" state	4	247.5°
State 4	"0" state	5	90.0°	State 12	"1" state	5	270.0°
State 5	"0" state	6	112.5°	State 13	"1" state	6	292.5°
State 6	"0" state	7	135.0°	State 14	"1" state	7	315.0°
State 7	"0" state	8	157.5°	State 15	"1" state	8	337.5°
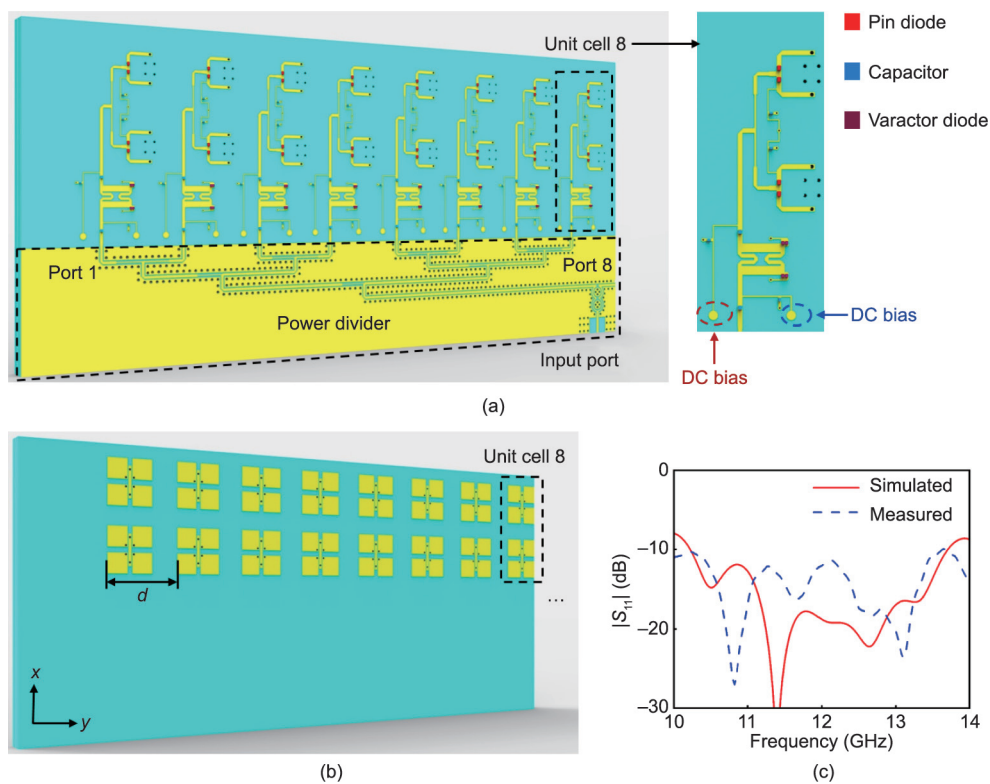
Fig. 6. Sketch of the proposed 4-bit array (only half of which is presented here) and $|S_{11}|$ of the 1:16 power divider. (a) Bottom view; (b) top view; (c) simulated and measured $|S_{11}|$ of the power divider.

ports at 12 GHz are 6° and 17°, respectively. As the measured phase error is partially caused by the SMA connectors' soldering, it may be smaller when the power divider is directly used in the array.

As exhibited in Figs. 6(a) and (b), in each row of the array, two 1-bit ME dipoles are used in parallel and are fed by a two-way equal-split power divider. The purpose of using parallel ME dipoles in each row is to increase the gain of the array. The miniaturized RTPS is integrated with the parallel ME dipoles, thereby constituting a digital coding radiation unit cell. Sixteen digital coding radiation unit cells are arranged along the H plane (the y–o–z plane), and the proposed 1:16 power divider is cascaded to them, thus forming the complete 4-bit array. To activate the pin and varactor diodes, two sets of DC bias circuits are introduced into each

Table 2
Calculated, simulated, and measured amplitude distributions of the power divider at 12 GHz.

Port	Amplitude distributions		
	Calculated	Simulated	Measured
1	0.38	0.37	0.41
2	0.43	0.44	0.44
3	0.52	0.55	0.55
4	0.65	0.69	0.66
5	0.78	0.78	0.81
6	0.89	0.91	0.91
7	0.96	0.97	0.99
8	1.00	1.00	1.00

radiation unit cell, in which the bias circuit (shown in the red dashed circle in the figure) supplies DC voltage to the 1-bit ME dipoles, and the other (shown in the blue dashed circle) is for the RTPS. To isolate DC and radio frequency (RF) signals, six 100 pF chip capacitors are used in each unit cell. The geometries of the DC bias circuits and the positions of the chip capacitors are well optimized in CST Microwave Studio to ensure that they have little influence on the performance of the array.

In order to steer the main beam in a specified direction, the quantized phase distribution on the 4-bit array should be calculated. Assuming that the array is scanned to an angle θ, then the required phase of the nth unit cell on the array can be expressed as follows:

$$\varphi_n = -k_0 d \cdot \sin\theta \cdot n, \; n = 1, 2, ..., 16 \tag{5}$$

where k_0 is the wavenumber in free space, and d is the distance between adjacent unit cells. The obtained φ_n is normalized within the range of 0° to 360°; then, it is quantized into 16 digital states according to the coding method:

$$\text{Code}_n = \begin{cases} 0, & 0° \leq \varphi_n \leq 22.5° \\ 1, & 22.5° \leq \varphi_n \leq 45° \\ & \vdots \vdots \\ 14, & 315° \leq \varphi_n \leq 337.5° \\ 15, & 337.5° \leq \varphi_n \leq 360° \end{cases} \tag{6}$$

Thus, the quantized phase of the nth unit cell is calculated as follows:

$$\varphi_{n,\text{qua}} = \frac{360°}{2^4} \cdot \text{Code}_n, \; n = 1, 2, ..., 6 \tag{7}$$

Although the digital coding method above provides a simplified scheme for reconfigurable beam steering, it will still introduce quantization errors. In addition, coupling effects exist among the unit cells, which will also affect the radiation performance of the array. Therefore, the coding sequences of the array need to be fur-

ther optimized. A particle swarm optimization (PSO) algorithm is exploited to optimize the coding sequences. The codes calculated by Eq. (6) are taken as the initial input values, and the sidelobe level at the scan angle θ is set as the optimization goal. The final optimized coding sequences of the array for different scan angles are given in Table 3. For simplicity, only cases where the array is scanned from 0° to 45° are shown here, and the cases scanned to negative angles are omitted due to the symmetry of the array's radiation layer. Fig. 7(a) plots the simulated radiation patterns of the scanning beams in the H plane at 12 GHz. The realized gain in the broadside direction is 15.7 dBi, and the scan gain loss is 2.6 dB for the 45° beam. The highest sidelobe level is –16.4 dB at a 20° scan angle, and the backlobe level is below –29 dB. Fig. 7(b) illustrates the simulated cross-polarization (y-polarized) level of the array, which remains lower than –23 dB.

4. Experimental verification

To validate the performance of the proposed design, an array sample was manufactured by means of standard PCB technology. The array's dimensions were $9.70\lambda_0 \times 2.00\lambda_0 \times 0.15\lambda_0$, where λ_0 is the free-space wavelength at 12 GHz. A photograph and enlarged views of the array sample are presented in Figs. 8(a) and (b). Measurements of the fabricated array were performed in an anechoic chamber; the detailed experiment configuration is illustrated in Fig. 8(c). The array was mounted with four M2 nylon screws on an acrylic support that was fixed on the test turntable. By using DuPont wires, DC bias voltages were supplied to the array to independently control the states of the pin and varactor diodes. As shown in the inset of Fig. 8(c), the DC voltage source was a triple-output DC power supply (model IT6302, ITECH), in which two channels were connected to a breadboard that utilized dual in-line package (DIP) switches to control the states of the pin diodes. The remaining channel was connected to a PCB that uses rheostats to control the states of the varactor diodes. Thus, the

Table 3
Coding sequences of the array for different scan angles at 12 GHz.

Scan angle	Unit cell 1	Unit cell 2	Unit cell 3	Unit cell 4	Unit cell 5	Unit cell 6	Unit cell 7	Unit cell 8	Unit cell 9	Unit cell 10	Unit cell 11	Unit cell 12	Unit cell 13	Unit cell 14	Unit cell 15	Unit cell 16
0°	7	7	7	7	7	7	7	7	7	7	7	7	7	7	7	7
10°	15	14	12	11	9	8	6	5	4	2	0	15	13	12	10	9
20°	11	6	4	1	14	11	8	5	2	15	12	9	6	3	0	13
30°	0	12	8	4	15	11	7	3	15	10	6	2	14	10	6	1
45°	6	0	9	3	13	7	1	11	5	15	9	3	13	7	2	12

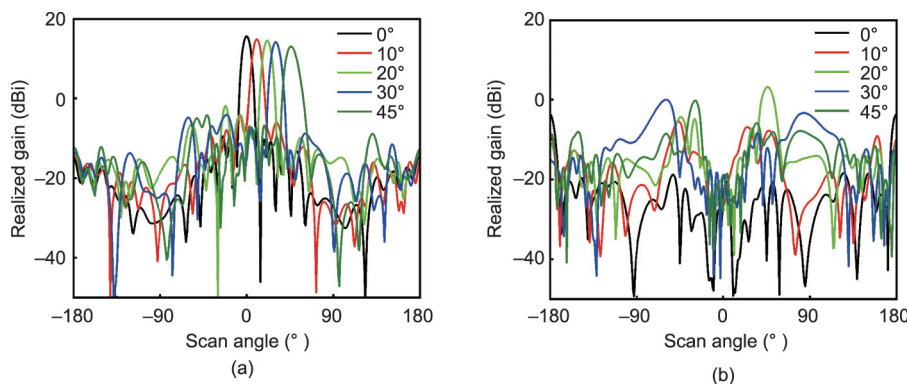Note: To be compact, the state "0" is abbreviated as 0, and so on.

Fig. 7. Simulated radiation patterns of scanning beams in the H plane at 12 GHz. (a) simulated co-polarization radiation patterns; (b) simulated cross-polarization radiation patterns.
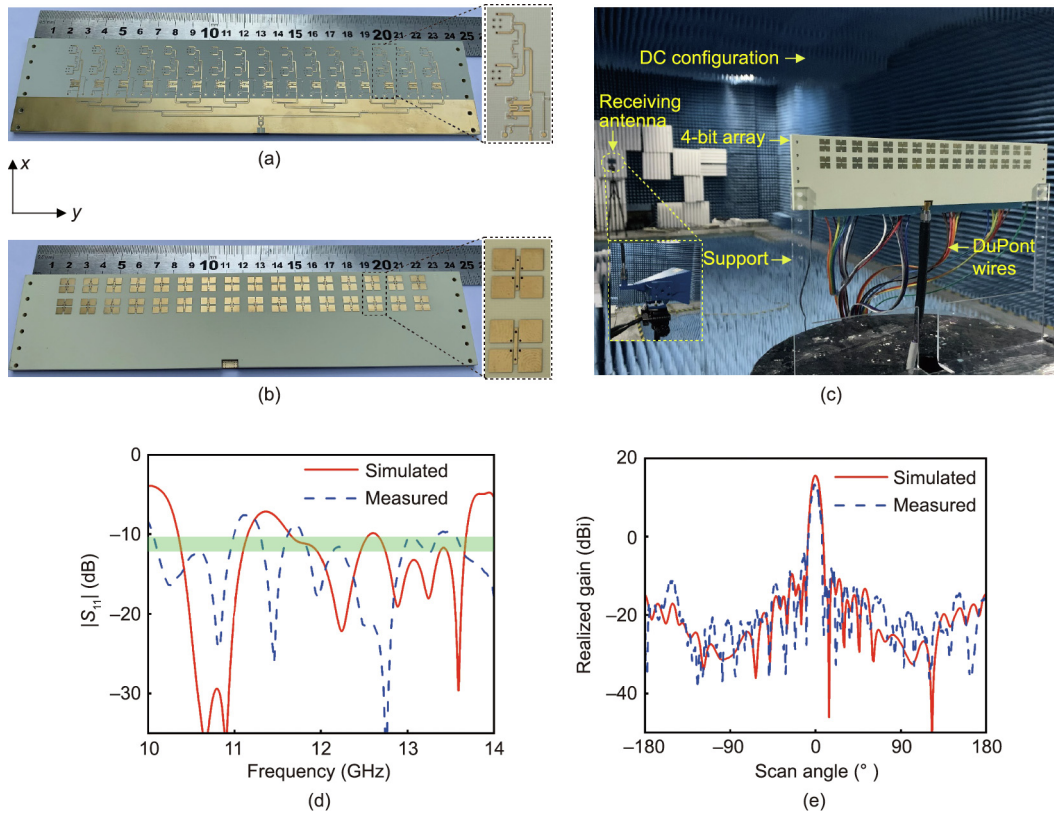
Fig. 8. (a) Bottom view and (b) top view of the fabricated array sample; (c) experimental configuration in the anechoic chamber; (d) simulated and measured $|S_{11}|$ of the broadside beam; (e) simulated and measured co-polarization radiation patterns of the broadside beam.

digital states of each radiation unit cell in the array could be tuned individually. As shown in the inset of Fig. 8(c), a horn operating from 9.8 to 15.0 GHz was used as the receiving antenna.

Fig. 8(d) exhibits the simulated and measured $|S_{11}|$ of the array at a 0° scan angle from 10 to 14 GHz. In the major portion of the frequency band, the measured $|S_{11}|$ is lower than –10 dB. The values deteriorate slightly around 11.1 GHz, which is consistent with the results shown in Figs. 4(c) and 6(c). The simulated and measured co-polarization patterns of the broadside beam are displayed in Fig. 8(e), and they are clearly in good agreement. It can be seen that the simulated and measured 3 dB beamwidths are 7.5° and 6.7°, respectively. The measured realized gain is 13.4 dBi, which is 2.3 dB lower than the simulated one. The measured radiation patterns from 0° to 45° are illustrated in Fig. 9, and the results validate the good scanning performance of the array. The sidelobe level is below –14.3 dB; this value is slightly lower than the simu-

lated result in Fig. 7(a), which can mainly be attributed to two factors: the insertion loss variation of the RTPS, as shown in Fig. 5(b); and the phase error of the 1:16 power divider. Moreover, the measured cross-polarization and backlobe levels are better than –23 and –25 dB, respectively. The gains and efficiencies of the broadside beam within the frequency band of interest are plotted in Fig. 10. It can be determined that the measured 3 dB gain bandwidth span is from 10 to 13 GHz (25%). In addition, the simulated and measured efficiencies at 12 GHz are 41.7% and 24.5%, respectively.

It should be pointed out that the values of the measured gain and efficiency decrease around 11.1 GHz, which is caused by the deterioration of $|S_{11}|$, as mentioned earlier. Compared with the simulated radiation efficiency, the decrease of the measured value can be attributed to the additional loss in the measurement, which is consistent with the results in Fig. 8(e). Table 4
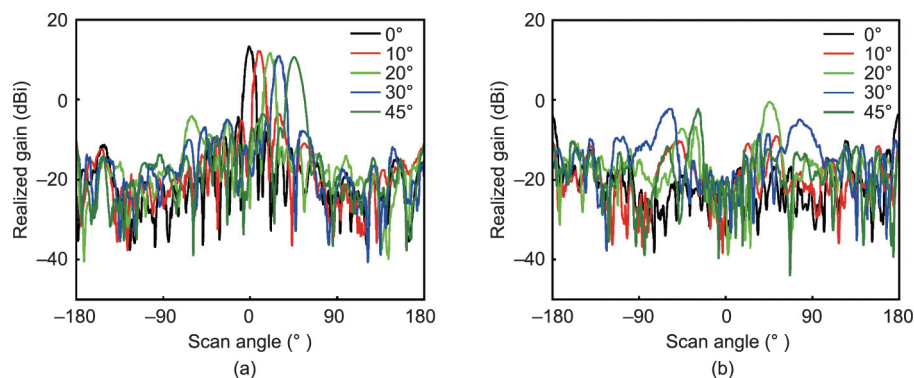

Fig. 9. Measured radiation patterns of scanning beams in the H plane at 12 GHz. (a) Measured co-polarization radiation patterns and (b) measured cross-polarization radiation patterns.

provides a gain loss analysis for the broadside beam at 12 GHz; it can be determined that the differences are caused by the following factors. First, there is loss of the SMA connector in the measurement, which is not present in the simulation, and the loss value is about 0.5 dB. Second, in the simulation, the real pin and varactor diodes are modeled by simple RLC circuits, resulting in a discrepancy between the simulated loss and the measured loss of the 1-bit ME dipole and RTPS. Third, there is a 0.8 dB difference between the simulated and measured results of the power divider, which is introduced by the manufacturing error. Finally, drift of the dielectric parameter and misalignment between the horn and antenna array can also cause a loss difference. Hence, the deviation of the efficiency can be improved by adopting a more accurate model of the pin and varactor diodes, utilizing finer fabrication technology, and optimizing the experimental setup in the future. Moreover, in order to improve the measured efficiency, better pin and varactor diodes can be used. Applying a series feed rather than a parallel feed can also help to improve the efficiency, but that will sacrifice the bandwidth of the array.

Fig. 11(a) compares the simulated and measured realized gains at 12 GHz within a 45° scan range. The measured realized gain decreases with the increasing scan angle, and the scan gain loss is 2.7 dB for the 45° beam in the H plane. The coupling among the antennas is significant for the array, since it influences the radiation performance, such as the gain, the sidelobe level, and the scan angle range. In order to study the coupling of the antenna array, the power divider of the array shown in Fig. 6 was removed; then, only port 8 was excited. The results of the coupling between the unit cells are plotted in Fig. 11(b). It was determined that the coupling between the antennas is small in the frequency band of interest, and the value is below –30 dB at 12 GHz. As discussed earlier, the power divider is composed of a GCPW, and the crosstalk among the different ports is small. Hence, the coupling of the whole array is small. Table 5 summaries the information of the array's scanning beams at 12 GHz. From the table, it can be seen that the beam pointing error is within 0.8°. In summary, the proposed planar 4-bit reconfigurable antenna array is demonstrated to have good performance, including excellent scanning capability, high gain, low sidelobe, and wide bandwidth.
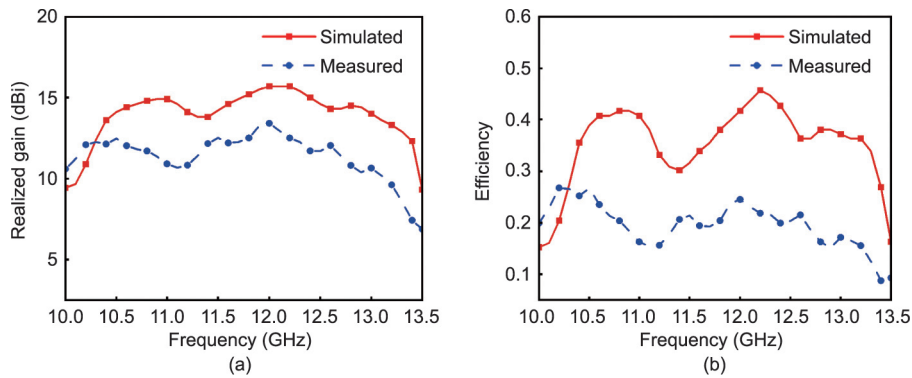

Fig. 10. (a) Simulated and measured realized gains of the broadside beam in the frequency band; (b) simulated and measured radiation efficiencies of the broadside beam in the frequency band.

Table 4
Gain loss analysis for the broadside beam at 12 GHz.

Result	Factors caused gain loss					
	Ideal directivity (dBi)	Realized gain (dBi)	Loss of RTPS (dB)	Loss of power divider (dB)	Loss of SMA connector (dB)	Loss of 1-bit ME dipole (dB)
Simulated	19.5	15.7	0.85	1.75	—	1.20
Measured	19.5	13.4	1.00	2.55	0.5	2.05[a]

[a] It contains the loss of 1-bit ME dipole and the loss due to the manufacturing and experimental errors.
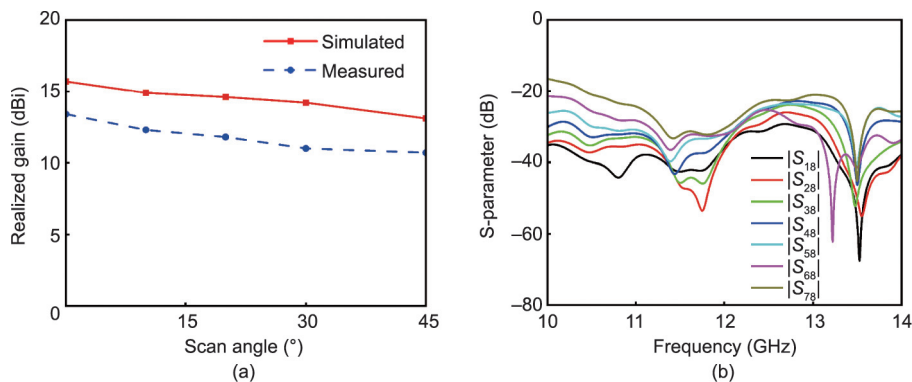

Fig. 11. (a) Simulated and measured realized gains for different scan angles; (b) coupling of the antenna array (the information for the ports is the same as that in Fig. 6).

Table 5
Information of the array's scanning beams in the H plane at 12 GHz.

Scan angle	Realized gain (dBi)		Sidelobe level (dB)		3 dB beamwidth (°)		Measured angle error (°)
	Simulated	Measured	Simulated	Measured	Simulated	Measured	
0°	15.7	13.4	−25.2	−17.8	7.5	6.7	0.8
10°	14.9	12.3	−19.1	−15.8	7.8	6.7	0.4
20°	14.6	11.8	−16.4	−16.1	8.1	6.7	0.5
30°	14.2	11.0	−18.3	−15.1	8.5	8.5	0
45°	13.1	10.7	−17.3	−14.3	10.8	10.5	0.5

5. Conclusions

The iconic feature of information metasurfaces is the use of digital states such as "0" and "1" to represent different electromagnetic responses, such as the phase responses. Based on this design philosophy, a planar 4-bit reconfigurable antenna array consisting of digital coding radiation elements was presented in this paper. The designed digital coding radiation element is composed of a 1-bit ME dipole and a miniaturized RTPS, which can provide 16 (2^4) digital states with 22.5° intervals for the array. In addition, a 1:16 power divider based on the Taylor aperture distribution is utilized to feed the array. A prototype of the array was fabricated and tested, and the measured results agreed well with the simulated ones. A scanning range of ±45° was demonstrated for the main lobe in the H plane, and the beam pointing error was less than 0.8°. The maximum measured realized gain was 13.4 dBi, with a corresponding radiation efficiency of 24.5% at 12 GHz. Moreover, the scan gain loss was 2.7 dB for the 45° beam. Good sidelobe and cross-polarization levels were obtained, with values below −14.3 and −23 dB, respectively. Furthermore, thanks to the use of the ME diploe, the backlobe level of the array was greater than −25 dB, and the measured 3 dB gain bandwidth of the broadside beam was 25%. With its outstanding features of good scanning and radiation characteristics, light weight, low cost, and low profile, the proposed array is expected to find significant applications in radar and wireless communication systems.

Compliance with ethics guidelines

Zheng Xing Wang, Hanqing Yang, Ruiwen Shao, Jun Wei Wu, Guobiao Liu, Feng Zhai, Qiang Cheng, and Tie Jun Cui declare that they have no conflict of interest or financial conflicts to disclose.

References

[1] Mailloux RJ. Phased array antenna handbook. 3rd ed. Norwood: Artech House; 2018.
[2] Stutzman WL, Thiele GA. Antenna theory and design. 3rd ed. Hoboken: John Wiley & Sons, Inc.; 2013.
[3] Ma Q, Cui TJ. Information metamaterials: bridging the physical world and digital world. PhotoniX 2020;1(1):1.
[4] Cui TJ, Li L, Liu S, Ma Q, Zhang L, Wan X, et al. Information metamaterial systems. iScience 2020;23(8):101403.
[5] Cui TJ, Qi MQ, Wan X, Zhao J, Cheng Q. Coding metamaterials, digital metamaterials and programmable metamaterials. Light Sci Appl 2014;3(10):e218.
[6] Wang ZX, Wu JW, Wu LW, Gou Y, Ma HF, Cheng Q, et al. High efficiency polarization-encoded holograms with ultrathin bilayer spin-decoupled information metasurfaces. Adv Opt Mater 2021;9(5):2001609.
[7] Zhang L, Chen XQ, Liu S, Zhang Q, Zhao J, Dai JY, et al. Space-time-coding digital metasurfaces. Nat Commun 2018;9(1):4334.
[8] Dai JY, Zhao J, Cheng Q, Cui TJ. Independent control of harmonic amplitudes and phases via a time-domain digital coding metasurface. Light Sci Appl 2018;7(1):90.
[9] Ma Q, Bai GD, Jing HB, Yang C, Li L, Cui TJ. Smart metasurface with self-adaptively reprogrammable functions. Light Sci Appl 2019;8(1):98.
[10] Li L, Cui TJ, Ji W, Liu S, Ding J, Wan X, et al. Electromagnetic reprogrammable coding-metasurface holograms. Nat Commun 2017;8(1):197.
[11] Li L, Ruan H, Liu C, Li Y, Shuang Y, Alù A, et al. Machine-learning reprogrammable metasurface imager. Nat Commun 2019;10(1):1082.
[12] Wu JB, Shen Z, Ge SJ, Chen BW, Shen ZX, Wang TF, et al. Liquid crystal programmable metasurface for terahertz beam steering. Appl Phys Lett 2020;116(13):131104.
[13] Zhao J, Yang X, Dai JY, Cheng Q, Li X, Qi NH, et al. Programmable time-domain digital-coding metasurface for non-linear harmonic manipulation and new wireless communication systems. Natl Sci Rev 2019;6(2):231–8.
[14] Cui TJ, Liu S, Bai GD, Ma Q. Direct transmission of digital message via programmable coding metasurface. Research 2019;2019:2584509.
[15] Zhang L, Chen MZ, Tang W, Dai JY, Miao L, Zhou XY, et al. A wireless communication scheme based on space- and frequency-division multiplexing using digital metasurfaces. Nat Electron 2021;4(3):218–27.
[16] Chen MZ, Tang WK, Dai JY, Ke JC, Zhang L, Zhang C, et al. Accurate and broadband manipulations of harmonic amplitudes and phases to reach 256 QAM millimeter-wave wireless communications by time-domain digital coding metasurface. Natl Sci Rev 2022;9(1):nwab134.
[17] Yang HH, Yang F, Xu SH, Mao YL, Li MK, Cao XY, et al. A 1-bit 10 × 10 reconfigurable reflectarray antenna: design, optimization, and experiment. IEEE Trans Antenn Propag 2016;64(6):2246–54.
[18] Yang HH, Yang F, Cao XY, Xu SH, Gao J, Chen XB, et al. A 1600-element dual-frequency electronically reconfigurable reflectarray at X/Ku-band. IEEE Trans Antenn Propag 2017;65(6):3024–32.
[19] Di Palma L, Clemente A, Dussopt L, Sauleau R, Potier P, Pouliguen P. Circularly-polarized reconfigurable transmitarray in Ka-band with beam scanning and polarization switching capabilities. IEEE Trans Antenn Propag 2017;65(2):529–40.
[20] Wang M, Xu SH, Yang F, Li MK. Design and measurement of a 1-bit reconfigurable transmitarray with subwavelength H-shaped coupling slot elements. IEEE Trans Antenn Propag 2019;67(5):3500–4.
[21] Wang Y, Xu SH, Yang F, Li MK. A novel 1 bit wide-angle beam scanning reconfigurable transmitarray antenna using an equivalent magnetic dipole element. IEEE Trans Antenn Propag 2020;68(7):5691–5.
[22] Hu J, Hao ZC, Wang Y. A wideband array antenna with 1-bit digital-controllable radiation beams. IEEE Access 2018;6:10858–66.
[23] Wang Q, Tian HW, Jiang WX, Chen MZ, Zhang XG, Cui TJ. An ultrawideband and dual-beam scanning array antenna characterized by coding method. IEEE Antennas Wirel Propag Lett 2020;19(12):2211–5.
[24] Zhang XG, Jiang WX, Tian HW, Wang ZX, Wang Q, Cui TJ. Pattern-reconfigurable planar array antenna characterized by digital coding method. IEEE Trans Antenn Propag 2020;68(2):1170–5.
[25] Chang L, Li Y, Zhang ZJ, Feng ZH. Reconfigurable 2-bit fixed-frequency beam steering array based on microstrip line. IEEE Trans Antenn Propag 2018;66(2):683–91.
[26] Liu PQ, Li Y, Zhang ZJ. Circularly polarized 2 bit reconfigurable beam-steering antenna array. IEEE Trans Antenn Propag 2020;68(3):2416–21.
[27] Smith M, Guo Y. A comparison of methods for randomizing phase quantization errors in phased arrays. IEEE Trans Antenn Propag 1983;31(6):821–8.
[28] Jiang W, Guo YC, Liu TH, Shen WF, Cao W. Comparison of random phasing methods for reducing beam pointing errors in phased array. IEEE Trans Antenn Propag 2003;51(4):782–7.
[29] Luk KM, Wong H. A new wideband unidirectional antenna element. Int J Microw Opt Technol 2006;1(1):35–44.
[30] Luk KM, Wu BQ. The magnetoelectric dipole—a wideband antenna for base stations in mobile communications. Proc IEEE 2012;100(7):2297–307.
[31] Balanis CA, editor. Modern antenna handbook. Hoboken: John Wiley & Sons, Inc.; 2008.
[32] Huang J. A technique for an array to generate circular polarization with linearly polarized elements. IEEE Trans Antenn Propag 1986;34(9):1113–24.

[33] Hall PS, Dahele JS, James JR. Design principles of sequentially fed, wide bandwidth, circularly polarized microstrip antennas. IEE Proc H 1989;136(5):381–9.

[34] Hu J, Hao ZC. A compact polarization-reconfigurable and 2-D beam-switchable antenna using the spatial phase shift technique. IEEE Trans Antenn Propag 2018;66(10):4986–95.

[35] Balthasar Mueller JP, Rubin NA, Devlin RC, Groever B, Capasso F. Metasurface polarization optics: independent phase control of arbitrary orthogonal states of polarization. Phys Rev Lett 2017;118(11):113901.

[36] Burdin F, Iskandar Z, Podevin F, Ferrari P. Design of compact reflection-type phase shifters with high figure-of-merit. IEEE Trans Microw Theory Tech 2015;63(6):1883–93.

[37] Singh A, Mandal MK. Electronically tunable reflection type phase shifters. IEEE Trans Circuits Syst II 2020;67(3):425–9.

[38] MADP-000907-14020W [Internet]. Lowell: MACOM Company; [cited 2021 Jul 9]. Available from: https://www.macom.com/products/product-detail/MADP-000907-14020W.

[39] Discover Simulia [Internet]. Paris: Dassault Systèmes; [cited 2021 Jul 9]. Available from: https://www.cst.com/products/cstmws.

[40] Sun J, Li A, Luk KM. A high-gain millimeter-wave magnetoelectric dipole array with packaged microstrip line feed network. IEEE Antennas Wirel Propag Lett 2020;19(10):1669–73.

[41] MAVR-011020-1411 [Internet]. Lowell: MACOM Company; [cited 2021 Jul 9]. Available from: https://www.macom.com/products/product-detail/MAVR-011020-1411.

[42] Pozar DM. Microwave engineering. 4th ed. Hoboken: John Wiley & Sons, Inc.; 2012.